

Substantially Improving Device Performance of All-Inorganic Perovskite-Based Phototransistors via Indium Tin Oxide Nanowire Incorporation

Yue Hou, Liming Wang, Xuming Zou,* Da Wan, Chang Liu, Guoli Li, Xingqiang Liu, Yufang Liu, Changzhong Jiang, Johnny C. Ho,* and Lei Liao*

All-inorganic halide perovskites (IHPs) have attracted enormous attention due to their intrinsically high optical absorption coefficient and superior ambient stabilities. However, the photosensitivity of IHP-based photodetectors is still restricted by their poor conductivities. Here, a facile design of hybrid phototransistors based on the CsPbBr_3 thin film and indium tin oxide (ITO) nanowires (NWs) integrated into a InGaZnO channel in order to achieve both high photo-responsivity and fast response is reported. The metallic ITO NWs are employed as electron pumps and expressways to efficiently extract photocarriers from CsPbBr_3 and inject electrons into InGaZnO . The obtained device exhibits the outstanding responsivity of $4.9 \times 10^6 \text{ A W}^{-1}$, which is about 100-fold better than the previous best results of CsPbBr_3 -based photodetectors, together with the fast response (0.45/0.55 s), long-term stability (200 h in ambient), and excellent mechanical flexibility. By operating the phototransistor in the depletion regime, an ultrahigh specific detectivity up to 7.6×10^{13} Jones is achieved. More importantly, the optimized spin-coating manufacturing process is highly beneficial for achieving uniform InGaZnO -ITO/perovskite hybrid films for high-performance flexible detector arrays. All these results can not only indicate the potential of these hybrid phototransistors but also provide a valuable insight into the design of hybrid material systems for high-performance photodetection.

1. Introduction

In the past decade, organic–inorganic metal halide perovskites (OMHPs) have drawn tremendous attention because of their extraordinary optoelectronic properties, including high

absorption coefficient, low exciton binding energy, long photogenerated carrier diffusion length, and tunable bandgap.^[1–4] It is unique that these hybrid perovskites can be easily made into high-quality films with the conventional fabrication technique of spin-coating, in which the process simplicity enables their potential use for numerous large-area and low-cost applications in solar cells and light emitting diodes.^[5,6] Besides, OMHPs have also been widely explored as active materials for high-performance photodetectors, which are important components for many modern communication and imaging systems.^[7–9] One of the essential requirements of photodetectors is to convert incident irradiation into electrical signals efficiently and reliably. However, photodetectors based on these hybrid perovskites still suffer from the issue of operational durability due to the chemical instability of organic monovalent cations in OMHPs, which greatly restricts their deployment for practical applications.

At the same time, the recent development of all-inorganic halide perovskites (IHPs), such as CsPbX_3 ($X = \text{I}, \text{Br}$, or Cl), have demonstrated the enhanced stability against moisture and heat as compared with their organic–inorganic hybrid counterparts.^[10–12] With the improved material stability, most

Dr. Y. Hou, Dr. D. Wan, Prof. L. Liao
School of Physics and Technology
Wuhan University
Wuhan 430072, China
E-mail: liaolei@whu.edu.cn

Dr. L. Wang, Prof. X. Zou, Dr. C. Liu, Prof. G. Li,
Prof. X. Liu, Prof. C. Jiang, Prof. L. Liao
Key Laboratory for Micro/Nano Optoelectronic Devices of Ministry
of Education & Hunan Provincial Key Laboratory of Low-Dimensional
Structural Physics and Devices
School of Physics and Electronics
Hunan University
Changsha 410082, China
E-mail: zouxuming@hnu.edu.cn

Prof. Y. Liu
Henan Key Laboratory of Infrared Materials
& Spectrum Measures and Applications
Henan Normal University
Xinxiang 453007, China

Prof. J. C. Ho
Department of Materials Science and Engineering
City University of Hong Kong
Tat Chee Avenue, Kowloon, Hong Kong SAR 999077, China
E-mail: johnnyho@cityu.edu.hk

 The ORCID identification number(s) for the author(s) of this article
can be found under <https://doi.org/10.1002/smll.201905609>.

DOI: 10.1002/smll.201905609

of the early works focused on the fabrication of IHP photodetectors utilizing the photovoltaic device structure. Owing to the poor conductivity of IHPS as well as the lack of appropriate photogain mechanism, the obtained IHP devices usually exhibit low responsivities (R) with the values of $\approx 10^{-1}$ to 10^1 A W^{-1} ,^[13–18] making the detection of weak optical signals difficult. To solve this problem, one alternative way is to employ the hybrid phototransistor structure by combining a high-mobility conducting layer with a perovskite light absorption layer. This way, the devices' responsivity can be greatly improved due to a strong photogating effect induced by trapped carriers in the perovskite layer. For example, hybrid graphene/MAPbI₃ and MoS₂/MAPbI₃ phototransistors have been developed and revealed with the high responsivities up to $\approx 10^6$ and $\approx 10^4 \text{ A W}^{-1}$,^[19,20] respectively, whereas TiO₂/MAPbI₃ heterostructures have also been investigated for the efficient photodetection.^[21] In any case, all of these studies heavily rely on the long lifetimes of trapped carriers in the MAPbI₃ layer (on the order of seconds to minutes) for the excellent responsivities, which inevitably give the slow response of the devices. Although the hybrid phototransistor based on MoS₂/CsPbBr₃ heterostructures can yield a much faster response of $\approx 1 \text{ ms}$ owing to the fewer trap states in the IHP layer, a much lower responsivity of 4.4 A W^{-1} is then resulted.^[22] Until now, it is still a grand challenge to achieve the low-cost and stable perovskite-based photodetectors with both ultrahigh sensitivity and fast response.

In this work, we perform a facile and rational design of high-performance hybrid phototransistors based on the CsPbBr₃ thin film and indium tin oxide nanowires (ITO NWs) integrated into the amorphous InGaZnO channel. To be specific, the metallic ITO NWs are employed as electron pumps to extract sufficient photocarriers from the perovskite layer into the InGaZnO film. Meanwhile, appropriate design of the corresponding band structure can further enable ITO to be an expressway of electrons in InGaZnO films to enhance the mobility of collected carriers. As a result, this hybrid phototransistor can deliver a substantially improved responsivity of $4.9 \times 10^6 \text{ A W}^{-1}$, an ultrahigh specific detectivity (D^*) of $7.6 \times 10^{13} \text{ Jones}$, together with fast response (rise/decay) times of $0.45/0.55 \text{ s}$. It is noted that this hybrid device can also be fabricated into a mechanically flexible photodetector, which exhibits the excellent stability upon bending test and exposure to ambient for 200 h. All of these results can not only evidently indicate the potential of these hybrid phototransistor structure based on all-inorganic perovskites, but also provide a valuable insight into the design of hybrid material systems for high-performance photodetection.

2. Results and Discussion

In general, phototransistors are operated based on the photogating effect.^[23–25] Distinctively, there is a heterojunction intrinsically formed within the hybrid phototransistor that is intentionally designed to separate the photogenerated electron-hole pairs. If one type of the photocarriers (e.g., holes) are trapped in the light absorption layer, the lifetime (τ_{lifetime}) of another carrier type (e.g., electrons) can then be prolonged in

the transport channel, inducing a high photogain (G) according to the following equation^[23]

$$G = \frac{\text{EQE} \times \tau_{\text{lifetime}}}{\tau_{\text{transit}}} \quad (1)$$

where EQE denotes external quantum efficiency of the device and τ_{transit} stands for transit time of the carriers transporting through the channel. Therefore, both photogain and response speed of the device are strongly related to the value of τ_{lifetime} such that a long trapping time of photocarriers would lead to a high photogain but a slow response. On the contrary, a short carrier trapping time usually gives a fast response but a poor photogain to the phototransistor. Considering the uncontrollability of τ_{lifetime} , we adopt a viable strategy to purposely design a hybrid CsPbBr₃-based phototransistor to improve the EQE/ τ_{transit} ratio together with the fast response. As shown in the device schematic in Figure 1a, the CsPbBr₃ film is used as the light absorption layer because of its better stability as compared with OMHPs as well as its impressively fast response as demonstrated in the previous works.^[22,26,27] Also, the sol-gel processed InGaZnO film is employed as the conducting layer in view of its low-temperature large-area processing capability, which is compatible with the typical manufacturing of perovskite thin films as well as phototransistors. In this case, there would be a type II band alignment established between CsPbBr₃ and InGaZnO, enabling the effective photocarriers separation at the InGaZnO/CsPbBr₃ interface (Figure 1b). For a typical phototransistor, the transit time can be estimated using the equation of^[28]

$$\tau_{\text{transit}} = \frac{L}{\mu_{\text{FE}} V_{\text{ds}}} \quad (2)$$

where L is the device channel length, μ_{FE} is the field-effect mobility, and V_{ds} is the source-drain bias. Although a relatively large V_{ds} or short L can ensure the τ_{transit} being small enough as compared with the τ_{lifetime} , it would inevitably induce the increased dark current.^[29,30] In contrast, improving the μ_{FE} value of InGaZnO transistor is more attractive here. For instance, our group recently developed a high-mobility InGaZnO field-effect transistor (FET) by incorporating ITO NWs into the channel.^[31] The low-frequency noise measurements demonstrated that there would result in the reduced trap states of the InGaZnO film, leading to a greatly improved device performance. With the 0.5 wt% ITO NWs incorporation, the composite device exhibits a peak electron mobility value of $83.9 \text{ cm}^2 \text{ V}^{-1} \text{ s}^{-1}$, which is much higher than that of the pristine device ($6.2 \text{ cm}^2 \text{ V}^{-1} \text{ s}^{-1}$) (Figure S1, Supporting Information). The typical transfer characteristics ($I_{\text{ds}}-V_{\text{gs}}$) of the InGaZnO and InGaZnO-ITO devices measured at $V_{\text{ds}} = 1 \text{ V}$ are also presented in Figure 1c. Upon CsPbBr₃ decoration, the FET performance of both devices are preserved but they come with a negative shift on the threshold voltage (V_{th}), suggesting an *n*-type doping effect in InGaZnO channel. Meanwhile, a slightly increased off-state current is also observed. This is probably due to the leakage current between gate and source-drain electrodes through the CsPbBr₃ layer (Figure S2, Supporting Information). Importantly, after CsPbBr₃ deposition, the μ_{FE}

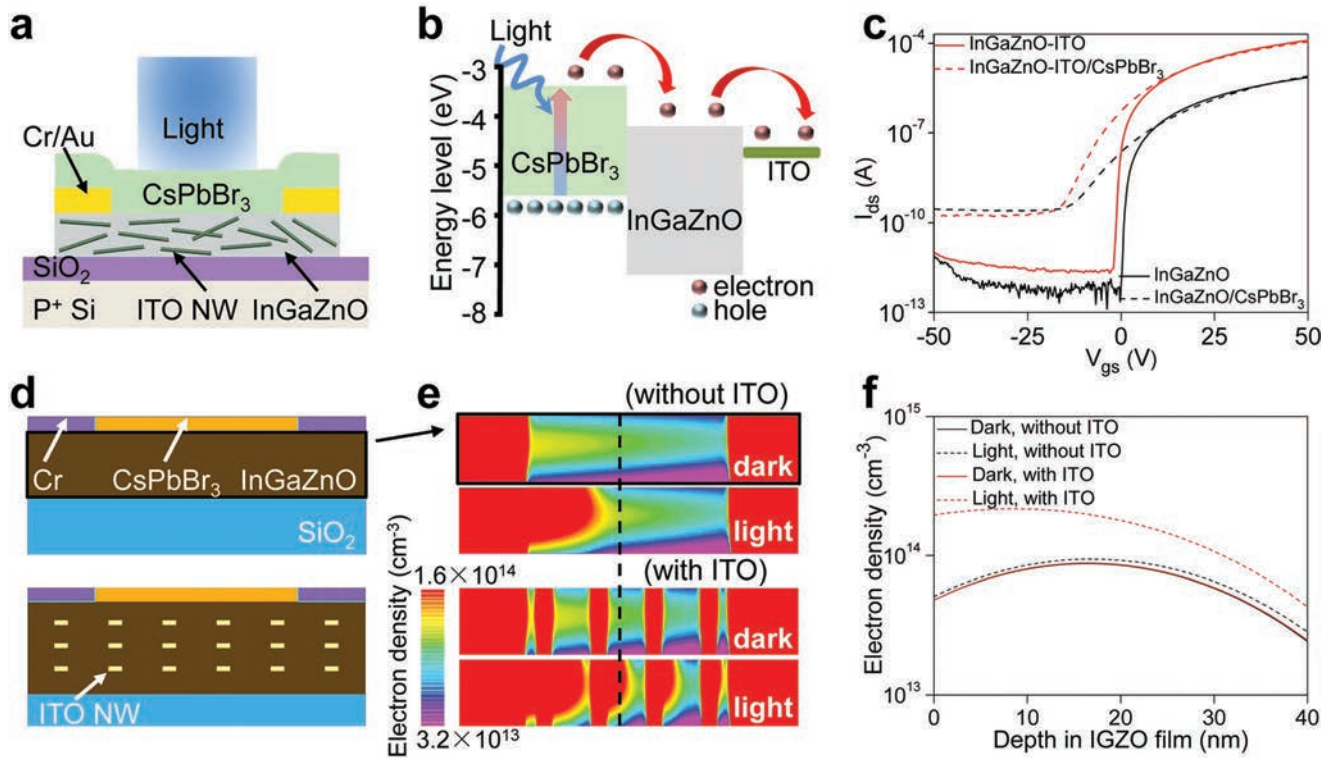


Figure 1. Structure and working principle of the InGaZnO-ITO/perovskite phototransistor. a) Structural schematic of the proposed device. b) Band diagram of the InGaZnO-ITO/perovskite heterostructure and corresponding photocarrier transfer under light illumination. c) Transfer characteristics of the InGaZnO and InGaZnO-ITO devices before and after CsPbBr₃ perovskite deposition. d) The device models for TCAD (Technology Computer Aided Design) simulation. e) TCAD simulations show the electron density in InGaZnO layer under dark and illumination, respectively. f) Electron density extracted along the dotted line in e. In comparison with the InGaZnO/perovskite device, the ITO NWs incorporation strongly increases the electron density under illumination.

value is almost unchanged ($6.2 \text{ cm}^2 \text{ V}^{-1} \text{ s}^{-1}$) for the InGaZnO/CsPbBr₃ device whereas slightly reduced to $76.7 \text{ cm}^2 \text{ V}^{-1} \text{ s}^{-1}$ for the InGaZnO-ITO/CsPbBr₃ device. This much higher carrier mobility of InGaZnO-ITO/CsPbBr₃ phototransistors would simply imply a much shorter response time (29 ns) there as compared with the one (263 ns) of InGaZnO/CsPbBr₃ devices.

Apart from the μ_{FE} improvement, the metallic ITO NWs can also be exploited as electron pumps to extract more photocarriers into the InGaZnO layer, which is beneficial for increasing the EQE value. In order to evaluate this electron pump effect, the simulations of photocarrier generation of the devices with and without ITO NW incorporation are performed as illustrated in the schematics in Figure 1d (see the Experimental Section for details). Upon illumination (457 nm) with a light intensity (P_{light}) of $10 \mu\text{W cm}^{-2}$, the photocarriers are first generated exclusively within the CsPbBr₃ layer, while fractions of these photogenerated electrons are subsequently transferred into the InGaZnO layer. The corresponding photogenerated holes would then be trapped in the CsPbBr₃ layer due to the charge traps existed within the CsPbBr₃ perovskite as well as the built-in potential established at the InGaZnO/CsPbBr₃ interface, leading to the formation of photogating effect until electron-hole recombination occurs (Figure 1e). When compared with dark equilibrium, electron density of InGaZnO layer increases under illumination. Once ITO NWs are incorporated into InGaZnO layer, enhanced electron accumulation would occur

in device channel (Figure 1f). Due to the decreased energy, fractions of photogenerated electrons in CsPbBr₃ layer can diffuse into ITO NWs through InGaZnO layer before recombination. This would induce a more efficient spatial separation of photocarriers at CsPbBr₃/InGaZnO interface, leading to a higher external quantum efficiency of the device. Combined with the above-discussed carrier mobility enhancement, photo-gain can be substantially improved for InGaZnO-ITO/CsPbBr₃ device.

In addition to the theoretical validation of the device performance enhancement, incorporating ITO NWs can also be easily achieved for the device fabrication. In this study, the ITO NWs were grown with a chemical vapor deposition method (see the Experimental Section for details). The corresponding high-resolution transmission electron microscopy (HRTEM) and selected area electron diffraction (SAED) images of ITO NW are shown in Figure S3 (Supporting Information), which illustrate its cubic crystal structure. In addition, the homogeneous distribution of In, Sn, and O atoms along the ITO NW body is also demonstrated using energy-dispersive X-ray spectrometry (EDS). The transfer curves of typical In₂O₃ NW devices with and without Sn doping are shown in Figure S4 (Supporting Information). Obviously, the neglectable gate modulated current indicates the NW being highly Sn doped. Utilizing these metallic ITO NWs, the entire fabrication process of the InGaZnO-ITO/CsPbBr₃ phototransistor is depicted in Figure 2a. The InGaZnO-ITO

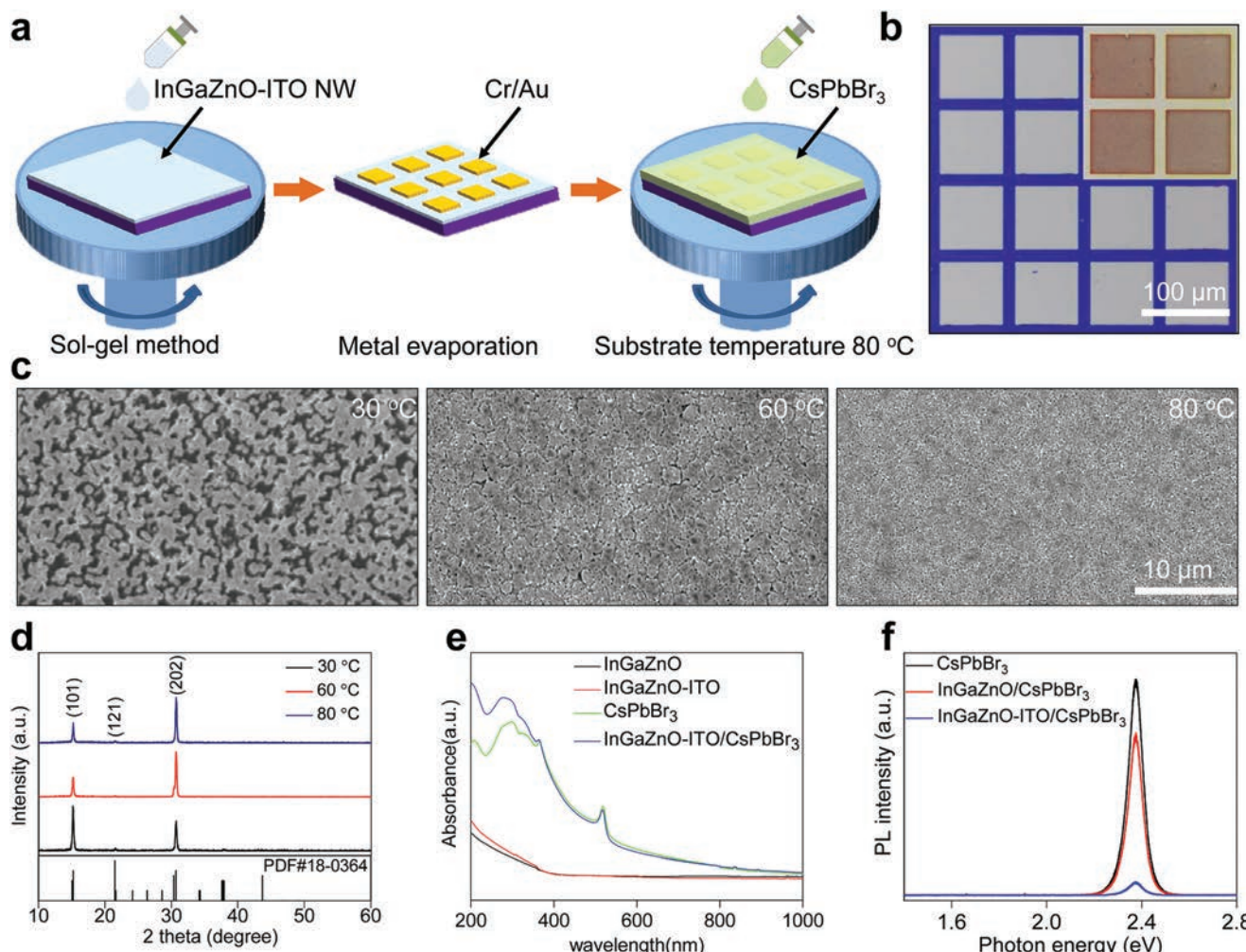


Figure 2. The fabrication process and characterization of the InGaZnO-ITO/perovskite phototransistor. a) Schematic illustration of the fabrication of InGaZnO-ITO/perovskite phototransistors. b) Optical images of the photodetector array before and after (inset) perovskite decoration. Scale bar is 100 μm . c) SEM images and d) XRD patterns of CsPbBr₃ film deposited onto the sol–gel processed InGaZnO-ITO film under different substrate temperatures. Scale bar is 10 μm . e) Absorption spectra of the InGaZnO-ITO, CsPbBr₃, and InGaZnO-ITO/perovskite films. f) PL spectra of the CsPbBr₃ film and the hybrid structures.

(0.5 wt% ITO NWs) composite film was first deposited onto a degenerately doped p-type silicon substrate with a 290 nm thick SiO₂ layer. Subsequently, Cr/Au (15/50 nm) electrodes were patterned on top of the composite film by thermal evaporation. Finally, the CsPbBr₃ film was deposited with dimethyl sulfoxide (DMSO) solution of PbBr₂ and CsBr (with a 1:1 mol ratio), and then the sample was annealed at 100 °C for 15 min to remove the residual DMSO. Figure 2b presents the corresponding optical images of InGaZnO-ITO FETs before and after perovskite deposition. It is well known that the film formation plays an important role in determining the film morphology and coverage, which in turn influences the fabricated device performance.^[32] Among many process parameters, the crystallization rate is a dominant factor dictating the film formation.^[33] In this case, since the commonly used DMSO has a relatively high boiling point, the crystallization of CsPbBr₃ is significantly slow; therefore, the low nuclei density is resulted, inducing the acicular structure and poor coverage of CsPbBr₃ film using the conventional one-step spin-coating method.^[34] In order to

alleviate this film quality issue as well as to improve the fabricated device performance, a thermally assisted fabrication scheme is then proposed to achieve a uniform and compact CsPbBr₃ film.

During the investigation of appropriate thermally assisted CsPbBr₃ film formation, it is found that the substrate temperature plays a crucial role in affecting the crystallization of CsPbBr₃. As shown in the scanning electron microscopy (SEM) images in Figure 2c, there are significant differences in the film morphology observed for different substrate temperatures, where the compact CsPbBr₃ film with a uniform grain distribution is produced with the relatively high substrate temperature of 80 °C. The cross-section SEM image further demonstrates a thinner but more uniform and compact film obtained with the thermally assisted film formation as compared with the thicker and discontinuous film using the conventional method (Figure S5, Supporting Information). Furthermore, X-ray diffraction (XRD) patterns were also collected for all the CsPbBr₃ films as presented in Figure 2d. It is clear that there are three

strong diffraction peaks located at 15.14° , 21.52° , and 30.68° , which are assigned to (101), (121), and (202) lattice planes, confirming the orthorhombic structure of CsPbBr_3 .^[35] Apparently, the substrate temperature is also witnessed to affect the preferential orientation of prepared films. For the films prepared at higher temperatures (60 and 80 °C), they have a preferential orientation following the (202) planes, which is in a distinct contrast to the one prepared at 30 °C. This is probably due to the formation of CsPbBr_3 phase using the high-temperature spin-coating process.

Besides the film morphology and crystallinity, it is also important to evaluate the optical absorption characteristics and photocarrier dynamics of all the samples. UV-vis absorption spectra of the pure InGaZnO , InGaZnO-ITO , pure CsPbBr_3 film, and hybrid $\text{InGaZnO-ITO/CsPbBr}_3$ films are presented in Figure 2e. There is no obvious change in light absorption range before and after ITO nanowires incorporation. The absorption edge of InGaZnO-ITO film is found to appear at 382 nm, corresponding to a band gap of 3.3 eV. As expected, the CsPbBr_3 film shows strong light absorption ability, especially in the UV region. Due to the superimposed effect, the absorption range of InGaZnO-ITO film is obviously extended after the formation of heterostructure with CsPbBr_3 . The corresponding photocarrier generation and transfer mechanism is also assessed by evaluating the photoluminescence (PL) spectra of CsPbBr_3 , InGaZnO/CsPbBr_3 , and $\text{InGaZnO-ITO/CsPbBr}_3$ (Figure 2f). Because of the efficient exciton dissociation and charge transfer at the InGaZnO/CsPbBr_3 interface, the reduced emission intensity is observed. Moreover, the PL quenching

effect of $\text{InGaZnO-ITO/CsPbBr}_3$ is particularly significant, which indicates the enhanced extraction of electrons. In this case, the photogenerated electrons are predicted to be extracted more efficiently to yield the higher EQE, while only few of them get recombined resulting in the high photoresponse for the hybrid $\text{InGaZnO-ITO/CsPbBr}_3$ Film.

After the photocarrier dynamics have been better understood, the optoelectronic performance of InGaZnO/CsPbBr_3 and hybrid $\text{InGaZnO-ITO/CsPbBr}_3$ phototransistors are then thoroughly investigated under light illumination. Figure 3a,b depict the device transfer characteristics under various illumination intensity with a V_{gs} sweeping from -50 to 50 V at $V_{\text{ds}} = 1$ V. As the P_{light} value increases, both off-state and on-state current of the $\text{InGaZnO-ITO/CsPbBr}_3$ phototransistor raise more than the ones of the InGaZnO/CsPbBr_3 device, indicating that the ITO NWs incorporation can effectively improve the device photoresponse. The ratio of output currents with and without light illumination ($I_{\text{light}}/I_{\text{dark}}$) can then be extracted from the transfer curves for both devices, in which this ratio is an important parameter typically used to evaluate the proportion of external signal to background noise. Generally, the higher $I_{\text{light}}/I_{\text{dark}}$ ratio represents the less obtrusive noise. As shown in Figure 3c, the $I_{\text{light}}/I_{\text{dark}}$ ratio of both devices is dramatically enlarged for the increasing incident light intensity. As compared with the InGaZnO/CsPbBr_3 device, the $I_{\text{light}}/I_{\text{dark}}$ ratio of $\text{InGaZnO-ITO/CsPbBr}_3$ device is increased by three orders of magnitude, achieving a maximum value of 3.4×10^4 at $V_{\text{gs}} = -17.5$ V even when P_{light} is as low as $104.1 \mu\text{W cm}^{-2}$. Without light illumination, the hybrid phototransistor operates

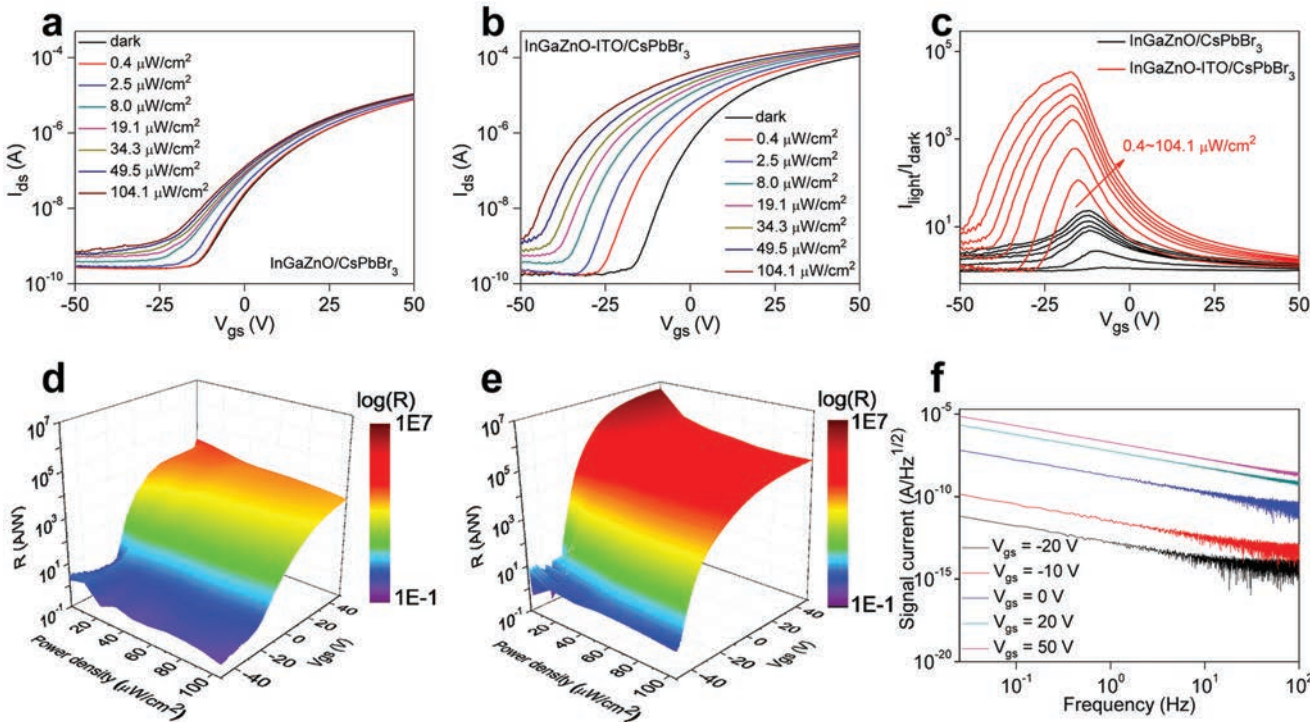


Figure 3. Optoelectronic characterization of the hybrid phototransistors under 457 nm laser illumination. $I_{\text{ds}}-V_{\text{gs}}$ characteristics of a) InGaZnO /perovskite and b) $\text{InGaZnO-ITO}/\text{perovskite}$ phototransistors under both dark and illuminated conditions. c) $I_{\text{light}}/I_{\text{dark}}$ ratio of the hybrid phototransistors. Responsivity of d) $\text{InGaZnO}/\text{perovskite}$ and e) $\text{InGaZnO-ITO}/\text{perovskite}$ phototransistors, respectively. f) Noise analysis of the $\text{InGaZnO-ITO}/\text{perovskite}$ phototransistor extracted from the Fourier transform of the dark current.

in an off-state mode for $V_{gs} = -17.5$ V, while the corresponding output current is very low. Under illumination, the device turns into an on-state operation with photogenerated electron injection into the channel whereas the output current amplifies significantly by the photogating effect. This way, the I_{light}/I_{dark} ratio of InGaZnO-ITO/CsPbBr₃ phototransistor can be simply enhanced with the higher illumination intensity.

In order to precisely evaluate the device photoresponse, responsivity can be calculated with the following equation^[28]

$$R = \frac{I_{light} - I_{dark}}{P_{light}S} = \frac{I_{ph}}{P_{light}S} \quad (3)$$

where I_{light} and I_{dark} denote the output currents with and without light illumination, respectively, I_{ph} stands for the photocurrent, and S refers to the active area of photodetector. As displayed in Figure 3d,e, the responsivities of both devices get increased with the increasing V_{gs} , which corresponds to the device operation manipulated from off-state to on-state. Meanwhile, the responsivities get reduced as the light intensity increases, which can be attributed to the enhanced photocarrier recombination with the increasing P_{light} . The highest responsivity of InGaZnO/CsPbBr₃ device is found to be 1.7×10^4 A W⁻¹ at $P_{light} = 0.4$ μW cm⁻². Once ITO NWs are incorporated into the device channel, the responsivity is greatly improved to 4.9×10^6 A W⁻¹. Notably, this responsivity is already 5 orders of magnitude higher than the ones of typical IPH photodetectors using photovoltaic structures,^[13–18] and 2 orders of magnitude higher than those of CsPbBr₃-based photogating devices.^[22,26,27,36] At the same time, it is also critical to assess the response time of the devices. For certain applications, such as video-rate imaging, the rise (decay) time is usually defined as the period for the photocurrent to rise (decay) from 10% to 90% (90% to 10%) of the final value. Accordingly, the rise time and decay time (τ_{rise} and τ_{decay}) are extracted to be 0.45 and 0.55 s, respectively (Figure S6, Supporting Information). This result is much faster than the ones previously reported for OMHPs-based hybrid phototransistors.^[19–21] Moreover, the gain of photodetector can be estimated according to the responsivity with the following equation^[37]

$$G = \frac{I_{ph}/q}{P_{light}/hv} = \frac{Rhc}{q\lambda} \quad (4)$$

where c denotes the speed of light, v denotes the incident photon frequency, and h stands for Planck's constant. In this case, the gain corresponding to the maximum responsivity is calculated to be 4.6×10^4 and 1.3×10^7 for InGaZnO/CsPbBr₃ and InGaZnO-ITO/CsPbBr₃ devices, respectively.

In addition to the responsivity, detectivity (D^*) is also an important parameter to compare the capability of photodetector in detecting weak optical signals. D^* can be estimated with the following equation^[37–39]

$$D^* = \frac{(SB)^{1/2}}{NEP} \quad (5)$$

$$NEP = \frac{\overline{i_n^2}^{1/2}}{R} \quad (6)$$

where B is the bandwidth, NEP is the noise equivalent power, and $\overline{i_n^2}^{1/2}$ is the root mean square value of the noise current. The gate electrodes in phototransistors can serve as sensitivity knobs to improve the D^* value by operating the devices in depletion regime. Figure 3f shows the measured $\overline{i_n^2}^{1/2}$ value at different V_{gs} values. It is clear that there is an obvious $1/f$ -noise component observed at $V_{gs} = 50$ V, while a flat line of spectral noise density starts to emerge at $V_{gs} = -20$ V due to the noise floor of the measuring instrument. Despite the high responsivity at $V_{gs} = 50$ V, the detectivity exhibits a relatively low value arising from the high noise value. Under $V_{gs} = -10$ V, the maximum D^* value is then extracted to be 7.6×10^{13} Jones at a frequency of 1 Hz (Figure S7, Supporting Information). This specific detectivity is superior than the value of traditional silicon-based photodetectors ($\approx 4 \times 10^{12}$ Jones).^[40]

In order to confirm the above device performance assessment, the device threshold voltage shift is plotted as a function of P_{light} (Figure 4a). For both devices, the threshold voltage are observed to shift toward the more negative values with the increasing power density. Because of the n type characteristic of InGaZnO, it is anticipated that the photogenerated holes are typically trapped, which induces a gating effect on the InGaZnO channel and leads to the boost of electron concentration there. In addition, the threshold voltage shift (ΔV_{th}) is highly depended on the power density, in which this relationship can be fitted well with the equation of $\Delta V_{th} \propto P_{light}^\alpha$, where α is a constant. The α value is then found to be 0.23 and 0.35 for the device with and without ITO NW incorporation, respectively. The non-unity exponent of $0 < \alpha < 1$ is often observed in photogating devices,^[41,42] as a result of the complex process of carrier generation, trapping, and recombination within semiconductors. The ΔV_{th} tends to saturate as the increase of the laser power, indicating that the net injection of photogenerated electrons has reached its maximum. This is partly due to the gradually filled trap states in perovskite. Once all the trap states are filled under a certain laser power, a stronger laser power would excite more free carriers that cannot be trapped. Therefore, the ΔV_{th} saturates. In general, when α equals 1, it represents a pure photoconductive effect, while α is less than 1, it indicates the existence of a photogating effect.^[41] Therefore, the smaller α value of InGaZnO-ITO/CsPbBr₃ device designates a more profound photogating effect here. Furthermore, the threshold voltage shift also provides an opportunity to evaluate the EQE value of measured devices (see the Experimental Section for details). It is observed that the InGaZnO-ITO/CsPbBr₃ device exhibits a peak EQE value of 57% at $P_{light} = 0.4$ μW cm⁻², which implies that $\approx 57\%$ of the incident photons are converted to trapped holes in CsPbBr₃, contributing to the photogating effect. This EQE value is about 17 times higher than that of the InGaZnO/CsPbBr₃ device (Figure 4b). According to Equations (1) and (2), the enhanced μ_{FE} and EQE with ITO NW incorporation would lead to a predicted amplification factor of ≈ 237 for the photogain, which is in good agreement with the measured value of ≈ 288 here. As shown in the energy band schematics in Figure 4c,d, the enhancement mechanism of device photogain can be understood in the following manner. Under light illumination, parts of the photogenerated electrons are transferred into the InGaZnO channel. The corresponding holes are then trapped in the CsPbBr₃ layer until carrier recombination occurs,

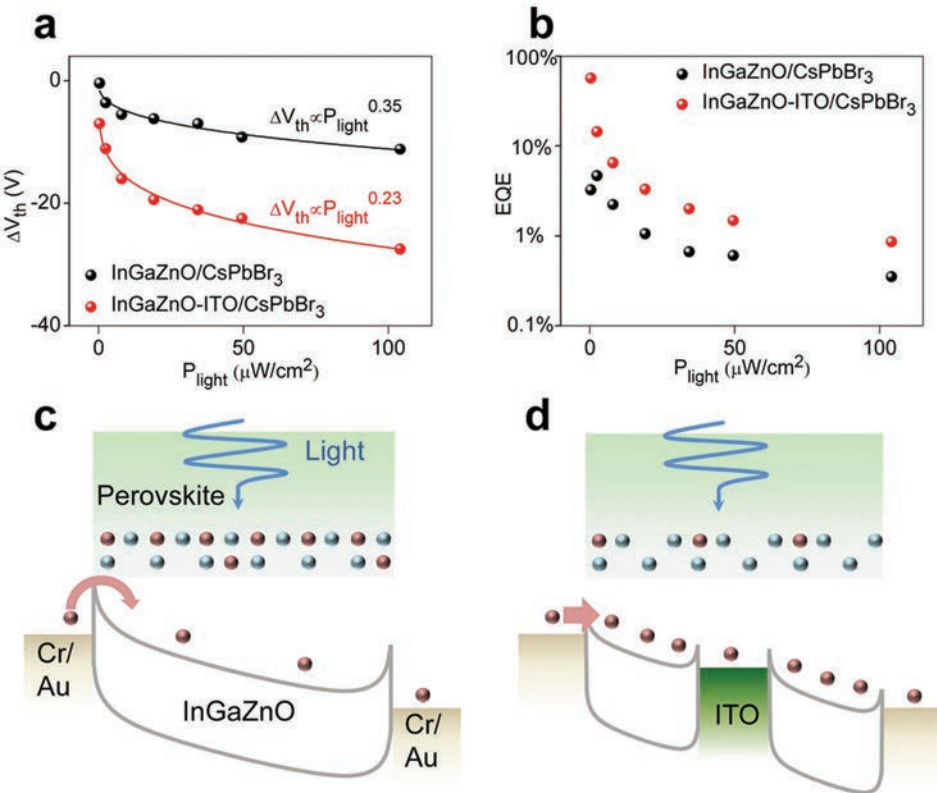


Figure 4. Performance comparison of InGaZnO/perovskite and InGaZnO-ITO/perovskite devices. a) The threshold voltage shift and b) external quantum efficiency as a function of laser power. Schematic illustration of the working mechanism of c) InGaZnO/perovskite and d) InGaZnO-ITO/perovskite devices.

which lower the Fermi level of InGaZnO, inducing the Schottky barrier reduction at the contact region. As a result, the ITO NW incorporation can lead to a substantial increment of both trapped holes and field-effect mobility of the phototransistor, resulting in the greatly enhanced photogain. To demonstrate the high performance achieved by InGaZnO-ITO/CsPbBr₃ phototransistor in comparison with the previously reported devices, we summarize the key performance parameters in Table S1 (Supporting Information). Among them, the hybrid InGaZnO-ITO/CsPbBr₃ device exhibits a high photosensitivity. However, in comparison with photovoltaic and photoresistance photodetectors, the response speed of InGaZnO-ITO/CsPbBr₃ degrades from tens of nanoseconds to hundreds of milliseconds, which is limited by trap-assisted photocarrier separation and recombination in photogating devices.

Recently, due to the proliferation of lightweight and portable electronics, flexible optoelectronic devices based on low-cost active materials and plastic substrates have received considerable attention.^[43,44] IPH-based flexible photodetectors have been achieved in previous reports, which exhibit excellent flexibility and stability.^[45,46] In this regard, in order to demonstrate the potential use of our devices for flexible applications, InGaZnO-ITO/CsPbBr₃ photodetectors were also constructed on polyimide substrates (Figure 5a). The fabricated devices were then electrically characterized with different bending angles (Figure 5b). Figure 5c presents the output characteristics of a typical flexible photodetector under different illumination intensities (457 nm). The maximum R value is extracted to be

$3.3 \times 10^4 \text{ A W}^{-1}$ at $V_{ds} = 5 \text{ V}$. Apparently, the output current remains almost unchanged after mechanically bending to an angle of 90°. The mechanical robustness of the device can be further assessed by the time-dependent photoresponse measurement upon 200 bending cycles (Figure 5d). Here, the rise time and decay time are extracted to be 0.28 and 0.61 s, respectively, which is similar to the value of rigid SiO₂ substrate. Furthermore, the spin-coating manufacturing process of these films can easily enable us to fabricate photodetector arrays, which is essential for the subsequent device integration. The output currents of a 5×5 photodetector arrays are then systematically characterized, where the collected signals are converted into a two-dimensional plot in order to display a contrast map (Figure 5e). It is evident that the devices exhibit a higher output current under illumination ($P_{\text{light}} = 104.1 \mu\text{W cm}^{-2}$), while they give a lower current under dark. The small device-to-device variation without any device failure can further illustrate the uniformity of these photodetector arrays. Importantly, the stability of these device arrays is as well monitored with the ambient exposure (30 °C and 50% humidity). Remarkably, the device photocurrent can maintain 85% of its initial value after 200 h of exposure, which clearly indicates its excellent long-term stability of the photodetector (Figure 5f).

3. Conclusion

In conclusion, through the incorporation of metallic ITO NWs, high-performance CsPbBr₃-based phototransistors with

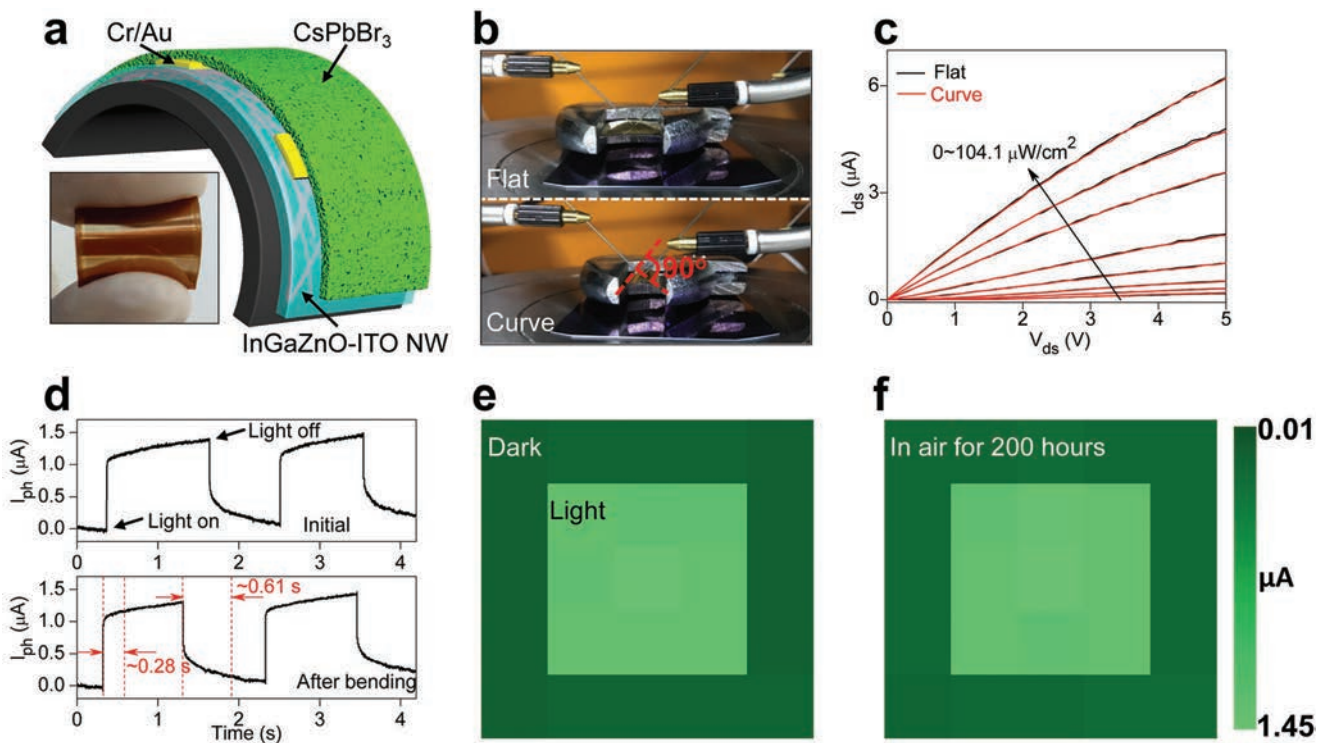


Figure 5. Flexibility and stability of the InGaZnO-ITO/perovskite phototransistors. a) Schematic of the flexible device structure. Inset is the corresponding optical image of devices fabricated on the polyimide substrate. b) Optical image of the flexible device during measurement at 0° and 90° of bending angles. c) Output curves of the device under various illumination intensities (457 nm). d) Time-dependent photoresponse of the device before and after 200 bending cycles. Contrast maps of the output current at $V_{ds} = 1$ V for 5×5 InGaZnO-ITO/perovskite photodetector arrays e) before and f) after 200 h of ambient exposure.

both high responsivity and fast response have been demonstrated for the first time. The top CsPbBr_3 layer can provide the excellent light absorption capability and ensure the fast response speed, while the hybrid InGaZnO-ITO film can be employed as an expressway for electron injection into the device channel. Owing to the enhanced external quantum efficiency, improved carrier mobility, and optimized CsPbBr_3 film coverage for the InGaZnO-ITO/ CsPbBr_3 phototransistor, these gate-tunable devices exhibit the outstanding responsivity ($4.9 \times 10^6 \text{ A W}^{-1}$), high detectivity (7.6×10^{13} Jones), large $I_{\text{light}}/I_{\text{dark}}$ ratio (3.4×10^4), and fast response time (0.45/0.55 s). More importantly, the optoelectronic performance of fabricated devices is very robust even after exposed to air for 200 h or upon 200 bending cycles. The overall device performance is more superior than other IHP-based photodetectors previously reported. The device architecture demonstrated here can be further applied to other perovskite-based hybrid devices for the enhanced photodetection performance.

4. Experimental Section

Device Fabrication: The ITO NWs were synthesized using the chemical vapor deposition method. A powder mixture of indium oxide, tin oxide, and graphite (with a weight ratio of 10:1:2) was placed into a quartz tube reactor. The silicon substrate covered with the gold catalyst was placed at the downstream next to the evaporation source. To start the growth, the evaporation source was heated to 1100 °C in 30 min under a 200 sccm gas flow (argon/oxygen = 100:1). After the quartz tube reactor

reached 1100 °C, the growth lasted for 30 min. Then, the quartz tube cooled naturally to room temperature, and a mass of ITO NWs were obtained on the silicon substrate surface.

The InGaZnO-ITO composite thin films were prepared from mixtures of InGaZnO sol-gel precursor and ITO NWs. Firstly, a 0.03 M InGaZnO sol-gel precursor was obtained by dissolving zinc acetate dehydrate, indium nitrate hydrate, and gallium nitrate hydrate with a molar ratio of 3:3:1 in 2-methoxyethanol. Then, the pre-synthesized ITO NWs were introduced into InGaZnO precursor in varying weight proportions by ultrasonication (20 s) in order to achieve a uniform dispersion of InGaZnO-ITO NWs composite precursor. Finally, the InGaZnO-ITO NWs composite thin films were obtained by spin-coating the composite precursor onto the substrate. The InGaZnO-ITO NWs FETs were fabricated by a two-step photolithography. A first photolithography and wet etch process were used to divide the as-prepared InGaZnO-ITO NWs thin films into isolated pads. After that, photolithography, vacuum thermal evaporation, and lift-off process were subsequently carried out to obtain FET devices with Cr/Au (15 nm/50 nm) source and drain electrodes. The channel length and width of the phototransistor were 15 and 70 μm , respectively.

For the preparation of CsPbBr_3 layer, CsBr and PbBr_2 (with a molar ratio of 1:1) were first dissolved in DMSO solution. Then, the mixture was stirred at room temperature for 6 h to obtain the precursor solution. The concentration of CsPbBr_3 was 0.4 M. Subsequently, the obtained solution was deposited onto the InGaZnO film by spin-coating at 3000 rpm for 1 min. Finally, the devices were heated at 100 °C for 15 min.

Material Characterization and Device Measurement: The CsPbBr_3 film morphologies were characterized with SEM (JEOL 6510). UV-vis absorption spectra were collected using a Shimadzu UV-2550. XRD measurement was performed at room temperature using the Rigaku SmartLab X-ray Diffractometer. Steady-state PL was measured with

an excitation laser of 325 nm. Electrical and optoelectronic device characterizations were performed by employing a semiconductor parameter analyzer (Agilent B1500A) and a standard probe station. The light source was a laser with the wavelength of 457 nm.

Evaluation of External Quantum Efficiency: Considering the photocarrier separation occurred at the InGaZnO/CsPbBr₃ interface, the number of electrons injected into InGaZnO channel (Δn) was equal to the trapped holes accumulated in the CsPbBr₃ layer. According to parallel plate capacitor model, the unit-area gate capacitance (C_{ox}) was calculated to be 11.9 nF cm⁻². Thus, a -7 V shift in V_{th} at $P_{light} = 0.4 \mu\text{W cm}^{-2}$ implies that the injected electron density from CsPbBr₃ to InGaZnO could be calculated by using the equation $\Delta n = C_{ox}\Delta V_{th}/q$, where the electron injection was estimated to be $5.2 \times 10^{11} \text{ cm}^{-2}$. Meanwhile, a power density of $0.4 \mu\text{W cm}^{-2}$ corresponding to a photon flux of $9.2 \times 10^{11} \text{ cm}^{-2} \text{ s}^{-1}$ was used. Since the complete decay time of photocurrent was ≈1 s (see Figure S5, Supporting Information), under the illumination of $0.4 \mu\text{W cm}^{-2}$, there would be 57% of the incident photons being converted into trapped holes in the CsPbBr₃ layer, which contributed to the photogating effect.

Device Simulation: Device simulation was carried out by using Silvaco TCAD. DevEdit module was used to design the device structure. In view of the intrinsic traps (e.g., oxygen vacancies, zinc-related acceptors and others) of IGZO, Shockley-Read-Hall recombination model was employed. The optical wavelength of the source beam was set to 457 nm and the power density was $10 \mu\text{W cm}^{-2}$. The thickness of InGaZnO and perovskite used in the simulation were set to 40 and 100 nm, respectively. The bandgap of InGaZnO and perovskite were set to 3.3 and 2.2 eV, while the relative dielectric permittivity of InGaZnO and perovskite were set to 4 (ref. [47]) and 41 (ref. [48]), accordingly. ITO nanowires were set to have an electron concentration of $1 \times 10^{20} \text{ cm}^{-3}$, a band gap of 2.8 eV, a relative dielectric permittivity of 9.3, an affinity of 4.6 eV, a m_e^* value of 0.25 m_0 , and m_h^* value of 0.24 m_0 ^[49]. Here, the m_e^* , m_h^* , and m_0 denote the electron effective mass, hole effective mass, and free electron mass, respectively. The work function of the electrode was 4.45 eV. Device operation temperature was chosen as 300 K as stated in the default set up. Fermi-Dirac statistics were implemented to account for the carrier concentration.

Acknowledgements

Y.H. and L.W. contributed equally to this work. This work was financially supported by the National Key Research and Development Program of Ministry of Science and Technology (No. 2018YFB0406603), the National Natural Science Foundation of China (Grant Nos. 61925403, 61851403, 61811540408, 51872084, and 61704051), the Strategic Priority Research Program of Chinese Academy of Sciences (Grant No. XDB30000000), as well as the Natural Science Foundation of Hunan Province (Nos. 2017RS3021 and 2017JJ3033).

Conflict of Interest

The authors declare no conflict of interest.

Keywords

flexible, high responsivity, InGaZnO, perovskites, phototransistors

Received: October 1, 2019

Revised: November 25, 2019

Published online: January 3, 2020

[1] A. Kojima, K. Teshima, Y. Shirai, T. Miyasaka, *J. Am. Chem. Soc.* **2009**, *131*, 6050.

[2] S. D. Stranks, G. E. Eperon, G. Grancini, C. Menelaou, M. J. Alcocer, T. Leijtens, L. M. Herz, A. Petrozza, H. J. Snaith, *Science* **2013**, *342*, 341.

- [3] N. J. Jeon, J. H. Noh, W. S. Yang, Y. C. Kim, S. Ryu, J. Seo, S. I. Seok, *Nature* **2015**, *517*, 476.
- [4] J. Burschka, N. Pellet, S.-J. Moon, R. Humphry-Baker, P. Gao, M. K. Nazeeruddin, M. Graetzel, *Nature* **2013**, *499*, 316.
- [5] S. D. Stranks, H. J. Snaith, *Nat. Nanotechnol.* **2015**, *10*, 391.
- [6] Z.-K. Tan, R. S. Moghaddam, M. L. Lai, P. Docampo, R. Higler, F. Deschler, M. Price, A. Sadhanala, L. M. Pazos, D. Credgington, F. Hanusch, T. Bein, H. J. Snaith, R. H. Friend, *Nat. Nanotechnol.* **2014**, *9*, 687.
- [7] L. Dou, Y. Yang, J. You, Z. Hong, W.-H. Chang, G. Li, Y. Yang, *Nat. Commun.* **2014**, *5*, 5404.
- [8] Y. Zhao, K. Zhu, *Chem. Soc. Rev.* **2016**, *45*, 655.
- [9] Y. Fang, Q. Dong, Y. Shao, Y. Yuan, J. Huang, *Nat. Photonics* **2015**, *9*, 679.
- [10] J. Song, J. Li, X. Li, L. Xu, Y. Dong, H. Zeng, *Adv. Mater.* **2015**, *27*, 7162.
- [11] M. V. Kovalenko, L. Protesescu, M. I. Bodnarchuk, *Science* **2017**, *358*, 745.
- [12] Q. A. Akkerman, G. Raino, M. V. Kovalenko, L. Manna, *Nat. Mater.* **2018**, *17*, 394.
- [13] Z. Yang, Q. Xu, X. Wang, J. Lu, H. Wang, F. Li, L. Zhang, G. Hu, C. Pan, *Adv. Mater.* **2018**, *30*, 1802110.
- [14] X. Li, D. Yu, F. Cao, Y. Gu, Y. Wei, Y. Wu, J. Song, H. Zeng, *Adv. Funct. Mater.* **2016**, *26*, 5903.
- [15] W. Zheng, X. Xiong, R. Lin, Z. Zhang, C. Xu, F. Huang, *ACS Appl. Mater. Interfaces* **2018**, *10*, 1865.
- [16] C. X. Bao, J. Yang, S. Bai, W. D. Xu, Z. B. Yan, Q. Y. Xu, J. M. Liu, W. J. Zhang, F. Gao, *Adv. Mater.* **2018**, *30*, 1803422.
- [17] X.-W. Tong, W.-Y. Kong, Y.-Y. Wang, J.-M. Zhu, L.-B. Luo, Z.-H. Wang, *ACS Appl. Mater. Interfaces* **2017**, *9*, 18977.
- [18] H. Zhou, Z. Song, C. R. Grice, C. Chen, J. Zhang, Y. Zhu, R. Liu, H. Wang, Y. Yan, *Nano Energy* **2018**, *53*, 880.
- [19] Y. Lee, J. Kwon, E. Hwang, C.-H. Ra, W. J. Yoo, J.-H. Ahn, J. H. Park, J. H. Cho, *Adv. Mater.* **2015**, *27*, 41.
- [20] D.-H. Kang, S. R. Pae, J. Shim, G. Yoo, J. Jeon, J. W. Leem, J. S. Yu, S. Lee, B. Shin, J.-H. Park, *Adv. Mater.* **2016**, *28*, 7799.
- [21] Z. Zheng, F. Zhuge, Y. Wang, J. Zhang, L. Gan, X. Zhou, H. Li, T. Zhai, *Adv. Funct. Mater.* **2017**, *27*, 1703115.
- [22] X. Song, X. Liu, D. Yu, C. Huo, J. Ji, X. Li, S. Zhang, Y. Zou, G. Zhu, Y. Wang, M. Wu, A. Xie, H. Zeng, *ACS Appl. Mater. Interfaces* **2018**, *10*, 2801.
- [23] G. Konstantatos, M. Badioli, L. Gaudreau, J. Osmond, M. Bernechea, F. P. G. De Arquer, F. Gatti, F. H. Koppens, *Nat. Nanotechnol.* **2012**, *7*, 363.
- [24] X. Zou, Y. Li, G. Tang, P. You, F. Yan, *Small* **2019**, *15*, 1901004.
- [25] L. Wang, X. Zou, J. Lin, J. Jiang, Y. Liu, X. Liu, X. Zhao, Y. F. Liu, J. C. Ho, L. Liao, *ACS Nano* **2019**, *13*, 4804.
- [26] H. Liu, X. Zhang, L. Zhang, Z. Yin, D. Wang, J. Meng, Q. Jiang, Y. Wang, J. You, *J. Mater. Chem. C* **2017**, *5*, 6115.
- [27] X. Li, D. Yu, J. Chen, Y. Wang, F. Cao, Y. Wei, Y. Wu, L. Wang, Y. Zhu, Z. Sun, J. Ji, Y. Shen, H. Sun, H. Zeng, *ACS Nano* **2017**, *11*, 2015.
- [28] F. Koppens, T. Mueller, P. Avouris, A. Ferrari, M. Vitiello, M. Polini, *Nat. Nanotechnol.* **2014**, *9*, 780.
- [29] Z. Xu, C. Wu, A. Li, Y. Ma, G. T. Fei, M. Wang, *IEEE Electron Device Lett.* **2018**, *39*, 240.
- [30] C. Ma, Y. Shi, W. Hu, M.-H. Chiu, Z. Liu, A. Bera, F. Li, H. Wang, L.-J. Li, T. Wu, *Adv. Mater.* **2016**, *28*, 3683.
- [31] D. Wan, A. Abilz, M. Su, C. Liu, C. Jiang, G. Li, H. Chen, T. Guo, X. Liu, L. Liao, *IEEE Electron Device Lett.* **2017**, *38*, 1540.
- [32] D. W. deQuilettes, S. M. Vorpahl, S. D. Stranks, H. Nagaoka, G. E. Eperon, M. E. Ziffer, H. J. Snaith, D. S. Ginger, *Science* **2015**, *348*, 683.
- [33] Y. Zhou, O. S. Game, S. Pang, N. P. Padture, *J. Phys. Chem. Lett.* **2015**, *6*, 4827.

- [34] Q. Wang, Y. C. Shao, Q. F. Dong, Z. G. Xiao, Y. B. Yuan, J. S. Huang, *Energy Environ. Sci.* **2014**, *7*, 2359.
- [35] Y. Shen, C. Wei, L. Ma, S. Wang, X. Wang, X. Xu, H. Zeng, *J. Mater. Chem. C* **2018**, *6*, 12164.
- [36] Y. Chen, Y. Chu, X. Wu, O.-Y. Wei, H. Jia, *Adv. Mater.* **2017**, *29*, 1704062.
- [37] D. Shao, J. Gao, P. Chow, H. Sun, G. Xin, P. Sharma, J. Lian, N. A. Koratkar, S. Sawyer, *Nano Lett.* **2015**, *15*, 3787.
- [38] X. Liu, L. L. Gu, Q. P. Zhang, J. Y. Wu, Y. Z. Long, Z. Y. Fan, *Nat. Commun.* **2014**, *5*, 4007.
- [39] C. Xie, C. Mak, X. Tao, F. Yan, *Adv. Funct. Mater.* **2017**, *27*, 1603886.
- [40] E. Liu, M. Long, J. Zeng, W. Luo, Y. Wang, Y. Pan, W. Zhou, B. Wang, W. Hu, Z. Ni, Y. You, X. Zhang, S. Qin, Y. Shi, K. Watanabe, T. Taniguchi, H. Yuan, H. Y. Hwang, Y. Cui, F. Miao, D. Xing, *Adv. Funct. Mater.* **2016**, *26*, 1938.
- [41] C. Hu, D. Dong, X. Yang, K. Qiao, D. Yang, H. Deng, S. Yuan, J. Khan, Y. Lan, H. Song, J. Tang, *Adv. Funct. Mater.* **2017**, *27*, 1603605.
- [42] J. O. Island, S. I. Blanter, M. Buscema, H. S. J. van der Zant, A. Castellanos-Gomez, *Nano Lett.* **2015**, *15*, 7853.
- [43] X. Hu, X. Zhang, L. Liang, J. Bao, S. Li, W. Yang, Y. Xie, *Adv. Funct. Mater.* **2014**, *24*, 7373.
- [44] F. P. G. de Arquer, A. Armin, P. Meredith, E. H. Sargent, *Nat. Rev. Mater.* **2017**, *2*, 16100.
- [45] G. Tong, H. Li, D. Li, Z. Zhu, E. Xu, G. Li, L. Yu, J. Xu, Y. Jiang, *Small* **2018**, *14*, 1702523.
- [46] W. Deng, H. Huang, H. Jin, W. Li, X. Chu, D. Xiong, W. Yan, F. Chun, M. Xie, C. Luo, L. Jin, C. Liu, H. Zhang, W. Deng, W. Yang, *Adv. Opt. Mater.* **2019**, *7*, 1801521.
- [47] T. Kawamura, H. Uchiyama, S. Saito, H. Wakana, T. Mine, M. Hatano, K. Torii, T. Onai, in *IEDM Tech. Dig.*, IEEE, San Francisco, CA **2008**, p. 77.
- [48] Y. Rakita, N. Kedem, S. Gupta, A. Sadhanala, V. Kalchenko, M. L. Bohm, M. Kulbak, R. H. Friend, D. Cahen, G. Hodes, *Cryst. Growth Des.* **2016**, *16*, 5717.
- [49] Y.-W. Huang, H. W. H. Lee, R. Sokhoyan, R. A. Pala, K. Thyagarajan, S. Han, D. P. Tsai, H. A. Atwater, *Nano Lett.* **2016**, *16*, 5319.